

# A 3D Bioprinted In Vitro Model of Pulmonary Artery Atresia to Evaluate Endothelial Cell Response to Microenvironment

Martin L. Tomov, Lilanni Perez, Liqun Ning, Huang Chen, Bowen Jing, Andrew Mingee, Sahar Ibrahim, Andrea S. Theus, Gabriella Kabboul, Katherine Do, Sai Raviteja Bhamidipati, Jordan Fischbach, Kevin McCoy, Byron A. Zambrano, Jianyi Zhang, Reza Avazmohammadi, Athanasios Mantalaris, Brooks D. Lindsey, David Frakes, Lakshmi Prasad Dasi, Vahid Serpooshan,\* and Holly Bauser-Heaton\*

Vascular atresia are often treated via transcatheter recanalization or surgical vascular anastomosis due to congenital malformations or coronary occlusions. The cellular response to vascular anastomosis or recanalization is, however, largely unknown and current techniques rely on restoration rather than optimization of flow into the atretic arteries. An improved understanding of cellular response post anastomosis may result in reduced restenosis. Here, an in vitro platform is used to model anastomosis in pulmonary arteries (PAs) and for procedural planning to reduce vascular restenosis. Bifurcated PAs are bioprinted within 3D hydrogel constructs to simulate a reestablished intervascular connection. The PA models are seeded with human endothelial cells and perfused at physiological flow rate to form endothelium. Particle image velocimetry and computational fluid dynamics modeling show close agreement in quantifying flow velocity and wall shear stress within the bioprinted arteries. These data are used to identify regions with greatest levels of shear stress alterations, prone to stenosis. Vascular geometry and flow hemodynamics significantly affect endothelial cell viability, proliferation, alignment, microcapillary formation, and metabolic bioprofiles. These integrated in vitro–in silico methods establish a unique platform to study complex cardiovascular diseases and can lead to direct clinical improvements in surgical planning for diseases of disturbed flow.

## 1. Introduction

Additive manufacturing and 3D bioprinting technologies, in particular, have proven to be versatile tools to create a variety of high-resolution models with significant impact in basic science and translational applications.<sup>[1,2]</sup> Previously, we have been able to bioprint 3D models used for procedural planning for complex pulmonary artery (PA) stenosis and atresia based on a patient case of Tetralogy of Fallot (TOF) with major aortopulmonary collateral arteries (MAPCAs).<sup>[3]</sup> The ability to engineer complicated vascular structures and study flow disturbance patterns allow investigating ideal transcatheter and surgical procedures for various vascular recanalization or anastomosis procedures, such as total occlusion lesions in coronary artery disease. Restenosis is a major complication in both complex PA stenosis and coronary artery disease, but the exact cause and mechanism of its formation along these abnormal vessels is not known and is unpredictable.

M. L. Tomov, L. Ning, H. Chen, B. Jing, A. Mingee, S. Ibrahim, A. S. Theus, G. Kabboul, J. Fischbach, K. McCoy, A. Mantalaris, B. D. Lindsey, D. Frakes, L. P. Dasi, V. Serpooshan, H. Bauser-Heaton  
Department of Biomedical Engineering  
Emory University School of Medicine and Georgia Institute of Technology  
Atlanta, GA 30322, USA  
E-mail: vahid.serpooshan@bme.gatech.edu; BauserH@kidsheart.com  
L. Perez, K. Do, V. Serpooshan, H. Bauser-Heaton  
Department of Pediatrics  
Emory University School of Medicine  
Atlanta, GA 30322, USA  
S. R. Bhamidipati, B. A. Zambrano, R. Avazmohammadi  
J. Mike Walker '66 Department of Mechanical Engineering  
Texas A&M University  
College Station, TX 77843, USA

J. Zhang  
Department of Biomedical Engineering  
School of Medicine and School of Engineering  
University of Alabama at Birmingham  
Birmingham, AL G094, USA  
R. Avazmohammadi  
Department of Biomedical Engineering  
Texas A&M University  
College Station, TX 77843, USA  
B. D. Lindsey, D. Frakes  
School of Electrical and Computer Engineering  
Atlanta, GA 30322, USA  
V. Serpooshan, H. Bauser-Heaton  
Children's Healthcare of Atlanta  
Atlanta, GA 30322, USA  
H. Bauser-Heaton  
Sibley Heart Center at Children's Healthcare of Atlanta  
Atlanta, GA 30322, USA

 The ORCID identification number(s) for the author(s) of this article can be found under <https://doi.org/10.1002/adhm.202100968>

DOI: 10.1002/adhm.202100968

These, in turn, lead to lifelong complications related to restenosis and atresia of the arterial segments.<sup>[4–7]</sup> Thus, robust *in vitro* cellular models, capable of recapitulating the complex vascular geometry and flow, are needed to aid in prevention, intervention, and discovery of potential pathways for alteration of this disease state.<sup>[3]</sup>

3D bioprinting technologies can produce high fidelity patient-specific models of cardiovascular pathologies based on medical imaging tools. To date, two approaches of bioprinting, extrusion- and light-based printing, are frequently used for creating *in vitro* models of healthy and diseased tissues.<sup>[8,9]</sup> Extrusion bioprinting is based on using pressure to deposit strands, which build up the desired 3D construct based on a computer assisted design (CAD) model.<sup>[10–12]</sup> Light-based bioprinting borrows its methodology from digital light processing (DLP) and stereolithography apparatus (SLA), where light beams are used to trigger radical polymerization reaction to build the 3D constructs one layer at the time.<sup>[13–16]</sup> DLP/SLA bioprinters offer high resolution, as light-based crosslinking can get down to cell-sized voxels,<sup>[17,18]</sup> allowing to generate precise tissue microenvironments.<sup>[15,16]</sup> The speed of DLP printing is also relatively high, compared to extrusion techniques, owing to the layer-by-layer crosslinking.

Anatomically accurate printed vascular analogues that allow physiologic flow can be instrumental in improving our understanding of physiology and the pathophysiology of many vascular systems.<sup>[10,19–25]</sup> These engineered models can help establish robust *in vitro* platforms for disease modeling and drug screening. The inclusion of relevant cell types, such as endothelial cells (ECs) and smooth muscle cells (SMCs), within bioprinted constructs is essential not only to development, but also to the homeostasis of functional bioartificial vessels. As aberrant cellular behavior could induce *de novo* stenosis or promote postsurgical restenosis, identification of important cellular function regulators may offer strategic insights for better understanding and treatment of vascular atresia.

In this study, we present a patient-specific *in vitro* platform that sustains viable and functional cell cultures under physiological flow regimens. These bioprinted constructs can be used to develop novel therapeutic approaches to treat various vascular anomalies, specifically vascular stenosis. Patient imaging data, obtained via computed tomography (CT) or 3D rotational angiography, were used to generate 3D digital models of complex PA atresia, which were then 3D printed using resins, and DLP bioprinted using gelatin methacrylate (gelMA) hydrogels. Simplified bifurcation geometries were subsequently seeded with human umbilical vein ECs (HUVECs) and used to study cellular response to flow patterns, identified via different experimental and computational approaches.

## 2. Results

### 2.1. 3D Bioprinting of An *In Vitro* Model of Anastomosed PA Structure

Extrapolating from patient clinical data images of an adolescent (14 years old) MAPCA patient (Figure 1A,B and Video S1, Supporting Information) were used to generate the bifurcated anastomosed PA atresia constructs.<sup>[3]</sup> We used Autodesk Fusion to generate a simplified CAD concept of the vasculature

area of interest, including a patent vessel and an atretic vessel (Figure 1C, inset). A synthetic model was first printed based on the obtained CAD model, using a clear resin ink, containing two vessels that were anastomosed with a connection (conduit) channel (Figure 1C, bottom). Following the validation, we bioprinted the same 3D model in 20% gelMA using the Lumen X DLP bioprinter (Figure 1D).

### 2.2. Mechanical and Fidelity Analyses of 3D Bioprinted PA Constructs

Microindentation analysis demonstrated an elastic modulus ( $E$ ) ranging from 59 to 94 kPa for the bioprinted gelMA constructs, depending on the depth within the 3D structure (Figure 1E,H). Of note, modulus increased from the bottom surface (last layer printed) to top surface (first layer printed) of these gelMA constructs (Figure 1G). We next conducted a series of microindentation tests on the luminal surface of bioprinted channels (5 mm depth, 2 mm distance between indentation points). Generated heatmap showed a relatively wide range of modulus (40–120 kPa) along the channel structures (Figure 1H, Table S1, Supporting Information). The highest modulus regions were located toward the end (outlet) of patent channel, while the atretic channel exhibited mostly low-modulus areas. Fidelity assessment of bioprinted constructs was conducted in the micro (strand-level) and the bulk scales and normalized by the CAD measurement for each parameter. We obtained a strand diameter ratio ( $D_s$ ) of 1.2, strand angle ratio ( $\alpha_s$ ) of 1.0, strand uniformity ratio ( $U_s$ ) of 1.0, and interstrand area ratio ( $A_s$ ) of 0.9 (Figure S1, the Supporting Information). Bulk fidelity assessments showed a 1.6% error in the construct length ( $l$ ), 7.6% error in the width ( $w$ ), and 2.7% error in the height ( $h$ ) (Figure 1I). Further, 12.8% and 12.3% errors were measured for the channel area ( $A$ ) and circularity ( $C$ ), respectively. Printed channel uniformity was also at 1.9% error, compared to the CAD model (Figure 1I).

### 2.3. Particle Image Velocimetry (PIV) Analysis of Flow Hemodynamics in Bioprinted PA Models

We developed and utilized two PIV-based assays to measure flow patterns in the PA constructs (Figure 2, Videos S2–4, Supporting Information). First, we used an ultrasound PIV approach to generate comprehensive 3D maps of flow within 4× scaled gelatin-based models (Figure S2A–D, Supporting Information), including the aberrant eddies and turbulent areas that are characteristics of stenotic-prone areas in anastomotic model (Figure 2A–D). The results demonstrated that the 2D in-plane flow velocity measurement can be obtained at a spatial sampling spacing of 0.38 mm (Figure 2C). The 3D velocity of the bifurcation flow in the gelatin model was obtained with a spatial spacing of 2.12 mm. The highest velocity was seen at the inlet near the anastomosis (i.e., in the region  $Z < 10$  mm and  $Y < 50$  mm, Figure 2D).

We subsequently used laser PIV to obtain more in-depth flow analysis of flow (Figure 2E, Figure S2E,F, Supporting Information). The mean velocity magnitude contour with in-plane vectors (Figure 2F, left) and instantaneous flow distributions were obtained (two examples at  $t = 0.13$  and  $0.37$  s are shown in

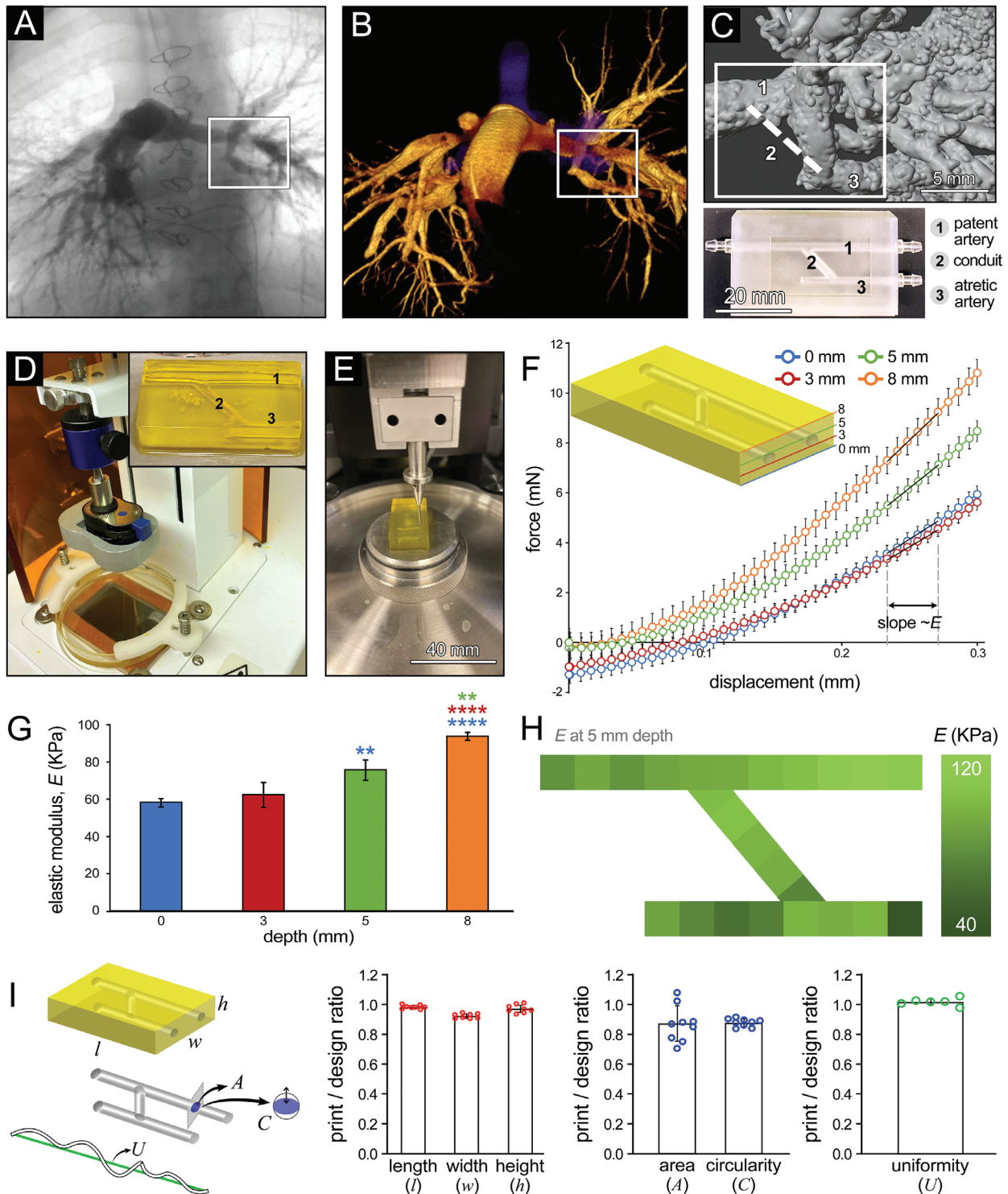


**Figure 1.** Hybrid PAA construct conceptualization, fabrication, and mechanical characterization. A) Patient imaging data was used to identify region of interest, specifically the atretic vessel and a neighboring patent vessel B). C, D) 3D geometry of the pathology area was generated C, top) and then a construct concept was extrapolated from the geometry and bioprinted C, bottom) using a stereolithography bioprinter D). E–H) Mechanical analysis of bioprinted gelMA constructs was conducted via a microindentation device E) on the surface, as well as different depths (0, 3, 5, and 8 mm) within the 3D hydrogel F). The unloading curves were subsequently used to calculate elastic modulus ( $E$ ) at each depth G). Finally, a heatmap of elastic modulus,  $E$ , was generated H) by conducting a series of microindentation tests throughout the printed channel structure (on the luminal surface). I) Fidelity measurements conducted by quantifying several structural features of printed gelMA constructs. These included external dimensions of the cubic construct (height,  $h$ , length,  $l$ , and width,  $w$ ), channel circularity ( $C = 4\pi A/p^2$ ), and channel uniformity ( $U$ ). A  $n = 4$ /experimental group was used for mechanical and fidelity assays. \*  $p < 0.05$ , \*\*  $p < 0.01$ , \*\*\*  $p < 0.001$  and \*\*\*\*  $p < 0.0001$ .

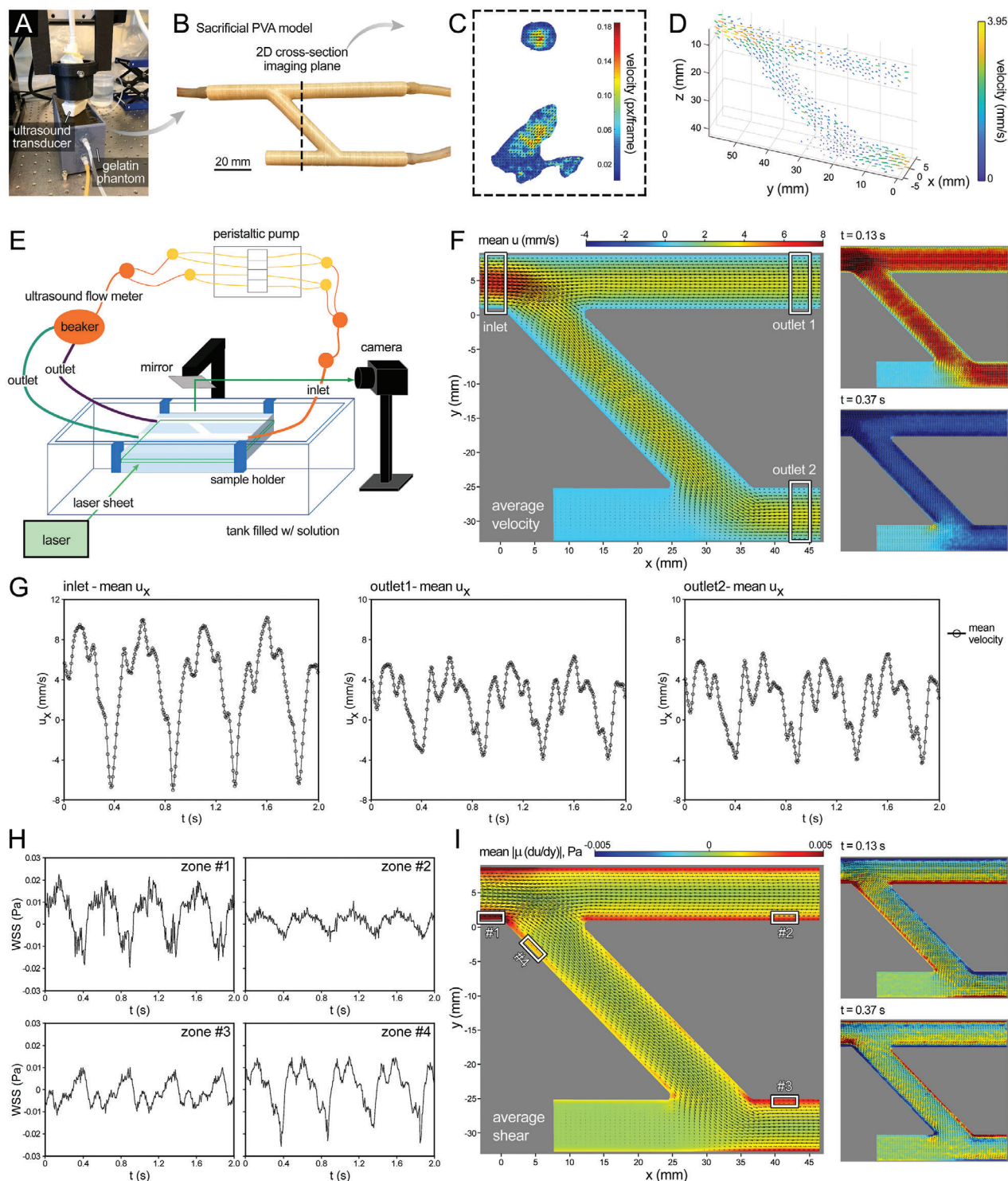


**Figure 2.** Particle image velocimetry (PIV) analysis of flow hemodynamics in bioprinted PAA constructs. A–D) Ultrasound PIV results for flow patterns within the PAA models. A) The ultrasound PIV setup used in this study. B) A 3D printed water soluble (sacrificial), polyvinyl acetate (PVA) model used at 4 $\times$  scale for the PIV measurements. C) Representative ultrasound-PIV 2D vector maps of the flow pattern shown for the highlighted cross-section (dashed line in B) within the PAA model. D) 3D reconstruction of flow velocity vectors within the entire construct. E–I) Laser PIV results of flow hemodynamics in PAA models. E) Schematic illustration of the experimental setup used. F) Averaged flow patterns generated during one cycle of peristaltic flow (left) and flow patterns at two specific time points ( $t = 0.13$  s, top right and  $t = 0.37$  s, bottom right). G) Mean velocity ( $u_x$ ) obtained by laser PIV at the inlet (left) and both outlets (middle and right) of the PAA model. H) Wall shear stress (WSS) profiles at 4 defined zones (#1–4) within the PAA geometry. I) Averaged shear ( $\mu$ ) patterns generated during one cycle of peristaltic flow (left) and shear patterns at two specific time points ( $t = 0.13$  s, top right and  $t = 0.37$  s, bottom right). The zones #1 to 4 with maximum alterations in shear are highlighted in the left panel in (I).

Figure 2F, right). These heatmaps showed the entrance of flow through the inlet and splitting rather evenly before exiting from the two outlets. The flow velocity ranged from  $-4$  to  $8 \text{ mm s}^{-1}$ . The time-varying mean flow rates for the inlet and two outlets (Figure 2G) were obtained by integrating the instantaneous velocity profiles (Figure S3A–C, Supporting Information) at corresponding locations. The flow pattern repeated itself every  $T = 0.492 \text{ s}$ . We next examined the mean shear in  $x$  direction (time-averaged absolute shear  $|\mu du/dy|$ ), as well as the wall shear stress (WSS) distribution in eight different zones within the 3D PA constructs (Figure 2H,I; Figure S3D,E, Supporting Information). The mean shear magnitude contour with in-plane vectors and two instantaneous shear distributions at  $t = 0.13$  and  $0.37 \text{ s}$  were obtained (Figure 2I), corresponding to the velocity heatmaps discussed above (Figure 2F). The shear stress ranged from  $-0.005$  to  $0.005 \text{ Pa}$ , with the greatest levels of shear alterations around the conduit (bridge) channel and its junction with the patent channel.

#### 2.4. Computational Fluid Dynamics (CFD) Analysis of Flow Hemodynamics in PA Constructs

CFD modeling was conducted for  $4\times$  scale (used for comparisons with PIV measurements; Figure 3 and Video S5, Supporting Information) and  $1\times$  scale (used for analysis in cell-laden bioprinted constructs; Figure S4 and Video S6, Supporting Information). A peristaltic flow rate waveform, adopted from the mean velocity measurements in the PIV experiments at  $4\times$  scale, was prescribed at the inlet boundary (Figure 3A). Mean velocities at the outlets exhibited consistent cyclic waveforms with values consistent with those measured in PIV (Figures 2G and 3A). Time-averaged (mean) velocity and representative snapshots of forward-reverse flow cycle indicated slightly reduced flow in the conduit compared to atretic and patent arteries (Figure 3B). In general, the velocity values predicted by CFD were in agreement with PIV measurements, although CFD results predicted a stronger flow gradient along the arteries than PIV measurements (Figure 3B). Zones 1 and 3, identifying the regions prior or subsequent to conduit, showed larger WSS values at peak forward-reverse velocities (Figure 3C,D). Although the flow is expected to become fully organized at peak velocities, flow recirculation was observed in Zone 4 (following the bifurcation), leading to lower WSS values (Figure 3D) and higher levels of oscillatory shear index (OSI) in this region (Figure 3E). Overall, CFD predictions for several measures of WSS (Figure 3C,D,F) showed both very quantitative and qualitative agreement with corresponding PIV estimates calculated from PIV measurements. The parabolic velocity profile prescribed at the inlet transitioned to nearly a plug flow at the outlets while maintaining the pulsatile flow condition (Figure 3G). Remarkably, these CFD predictions were also consistent with the corresponding PIV measurements (Figure S3A–C, Supporting Information). The velocity magnitude across the atretic artery outlet was slightly smaller than the patent artery outlet (Figure 3G), similar to the PIV measurements.

#### 2.5. Endothelialization of PA Models, In Vitro Perfusion, and Cellular Assays

To achieve reliable homeostatic flow of  $2 \text{ mL min}^{-1}$  within the constructs, customized housing chambers were 3D printed

and used to perfuse culture media through bioprinted artery models (Figure S5, Supporting Information) for the vascular analogues. Bioprinted gelMA models were (manually) cellularized with HUVECs and perfused in our bioreactor with no damage to the construct over the entire two-week time course (Figure S5, Supporting Information). We were able to reliably generate multiple bifurcation models, with a success rate of  $\approx 74\%$  ( $n = 16$ ) using the DLP bioprinting (Lumen X) and a success rate of  $\approx 60\%$  ( $n = 24$ ) using the extrusion-based bioprinting (BioAssemblyBot). The most common failure observed during DLP bioprinting was due to delamination in the 3D prints, likely caused by gelMA drying out during the rather long print times, while the most common cause of failure on the extrusion printer was excessive gelMA drying and construct cracking.

In situ noninvasive AlamarBlue metabolic activity assay demonstrated significantly (2–3 folds) higher levels of EC viability and growth in the printed constructs for up to 35 days in static culture, as compared to the control cast group (Figure 4A). We next assessed EC growth in the bioprinted PA constructs under static versus flow ( $2 \text{ mL min}^{-1}$ ) culture for 14 days. Printed constructs under flow culture demonstrated significantly (1.7–2 folds) greater levels of AlamarBlue reduction, suggesting higher levels of cell viability and growth (Figure 4B). We also compared EC growth in atretic versus precanalized (with the bridge) PA constructs, demonstrating significantly greater levels of AlamarBlue reduction in the bridged models (Figure S6A, Supporting Information). Subsequently, we examined the EC growth in the stented constructs (Figure S6B, Supporting Information). Cast and bioprinted PA models were stented on day 0 and then seeded with ECs. Long-term (56-day) culture of HUVECs in the stented constructs demonstrated fluctuating levels of AlamarBlue, with an increase in week 1, a decline in weeks 2–3, and an increase again after week 3 (Figure S6C, Supporting Information). At most time points, bioprinted models showed significantly greater levels of cell viability in comparison to cast constructs. Finally, we conducted stenting on day 9 of the in vitro culture, followed by another round of EC seeding for one of the groups. Results demonstrated a trend consistent with the long-term study above, with an initial increase in AlamarBlue (week 1), followed by a decline (weeks 2–3), and then rising back up and reaching a plateau (Figure S6C, Supporting Information). Reseeding constructs with ECs post stenting did not result in a significant increase in AlamarBlue readout compared to the control (no reseed) group.

Longitudinal bioprofiling assay demonstrated significant differences in nutrient consumption and metabolite production and accumulation in the 3D endothelial cultures under static versus dynamic flow conditions (Figure 4C,D). Specifically, the static cultures experienced statistically significant consumption of nutrients, glucose and glutamine (Figure 4C), with concomitant increase in metabolite accumulation, lactate and glutamate (Figure 4D) almost throughout the culture time, peaking at day 3. In contrast, the perfusion system, which constantly provides nutrients and removes metabolites, demonstrated almost constant levels of nutrients and metabolites (except for glutamine) which promotes the development of metabolically homeostatic environment and, to some extent, avoids the metabolic stress that was experienced in the static cultures.

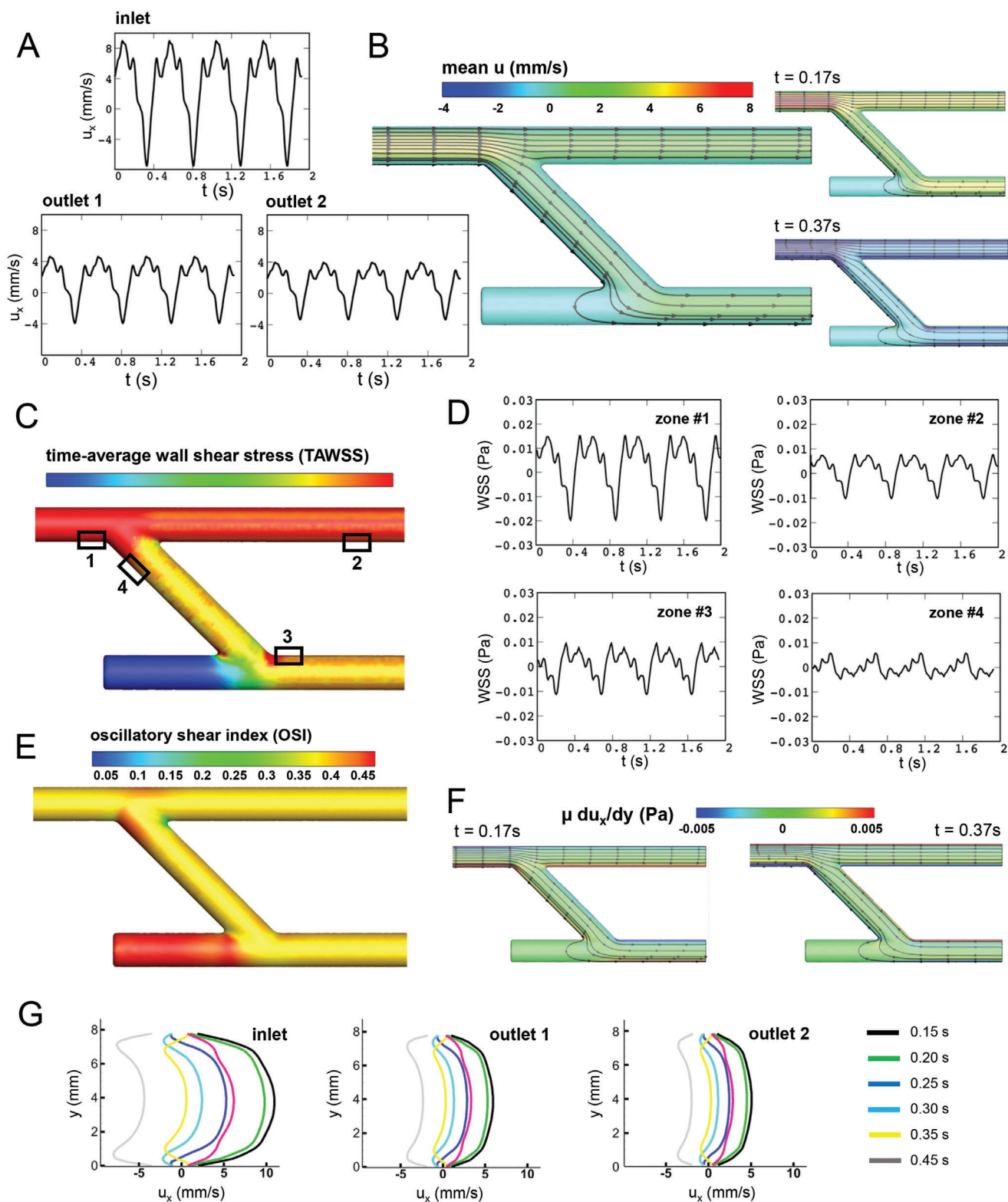
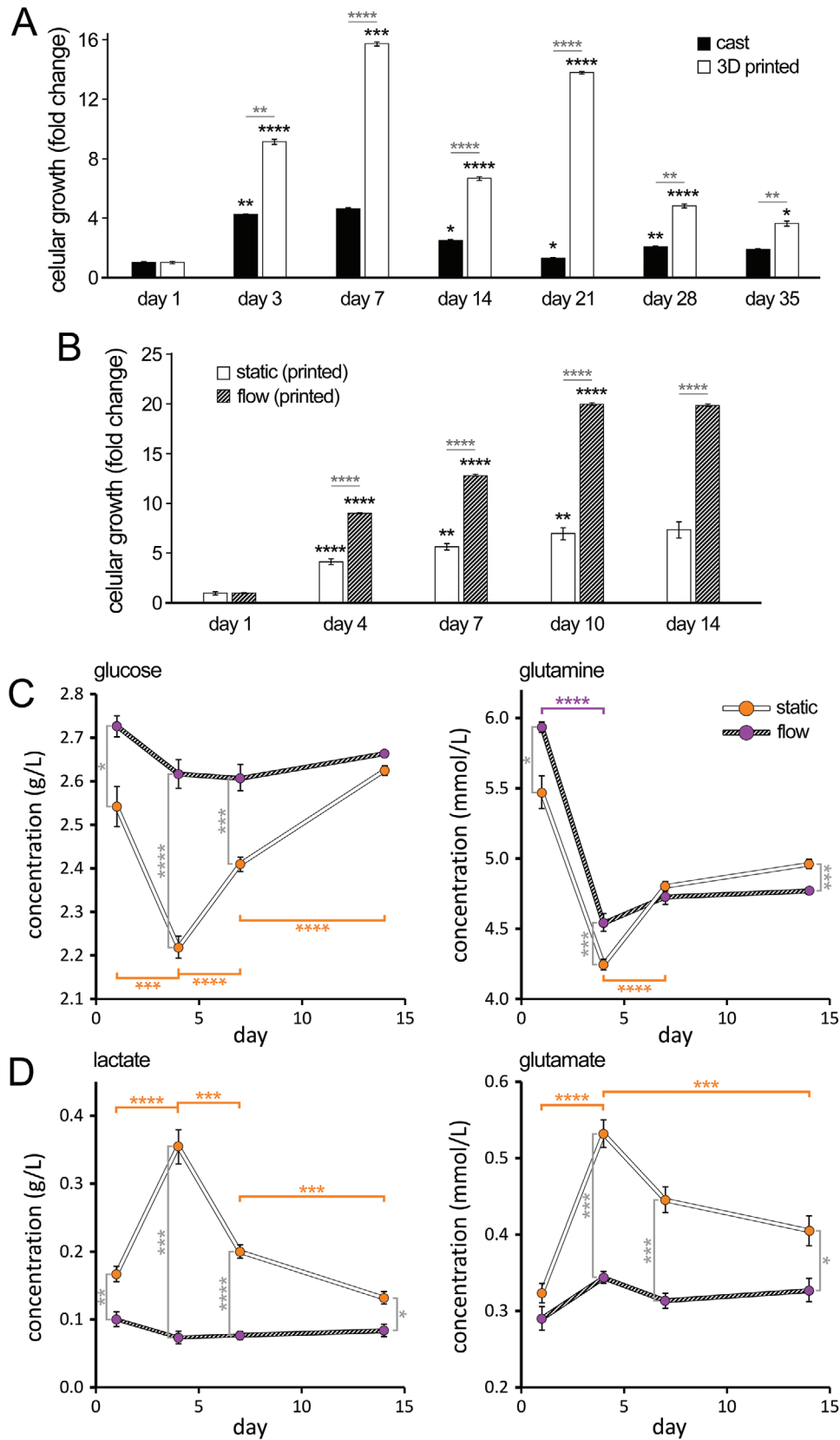


**Figure 3.** Computational fluid dynamics (CFD) modeling of flow within the bioprinted PAA construct at 4x scale. A) Average velocity values across the inlet and two outlets as a function of time for multiple cycles. B) Contour plots and streamlines taken at the mid-plane cross-section showing time-averaged and peak forward-reverse velocity. C) Contour plot of time-averaged wall shear stress (WSS) estimated on the 3D wall. D) WSS (vector magnitude) estimated at the mid-plane cross-section for comparisons with PIV calculations at zones 1, 2, 3, and 4. E) Contour plot of the oscillatory shear index (OSI) indicating changes in the direction of the WSS vector. F) Contour plot of the shear stress at the mid-plane cross section for comparison with PIV analysis. G) Velocity profiles along the diameter ( $y$ ) at the inlet two outlet areas.



## 2.6. Immunohistochemical Analysis of Cellular PA Models

ECs seeded in bioprinted PA constructs were fixed after a two-week static or dynamic (flow) culture and analyzed via immunohistochemical (IHC) staining (Figure 5). Four specific zones (#1 to 4) within the PA geometry were defined (consistent with the PIV measurements) (Figure 5A) and examined via confocal microscopy. 3D cultures demonstrated consistent expression of EC-specific cell surface marker CD31 and the tight junction marker Connexin43 (CX43) (Figure 5B,D,E). The flow culture yielded significantly greater level of CX43 (1.6 $\times$ ) expression compared to the control group cultured under static conditions (Figure 5B). A rather uniform and continuous endothelium was formed along the printed channel walls in both groups, while noticeable differences were observed in the morphology and structure of the cells (Figure 5C–E). HUVECs in dynamic flow showed a more extensive penetration into the bulk gelMA tissue, a more elongated morphology and, and an orthogonal orientation to the PA walls (median angle of 73° in the flow versus 37° in static culture) (Figure 5C, arrows in Figure 5E; Figures S7 and S8, Supporting Information). ECs in perfused group also exhibited an increased sprout length and enhanced angiogenic activity (Figure 5E; Figure S9 and Table S2, Supporting Information).

## 3. Discussion

Our group has recently embarked on a series of bioprinting endeavors to develop new generations of patient-specific, cell-laden, in vitro models that recapitulate several microenvironmental aspects of the native cardiovascular tissue. These include bioprinted in vitro models of vascular anastomosis in single ventricle heart defects,<sup>[26]</sup> pulmonary vein stenosis,<sup>[27]</sup> PAA in Tetralogy of Fallot,<sup>[3]</sup> and developing human heart.<sup>[28]</sup> These works presented strong evidence that bioprinted constructs could greatly aid examining cardiovascular processes in a temporally and spatially controlled manner in vitro while maintaining physiological/pathophysiological flow patterns. In this study, we investigated the use of a bioprinted model of canalized PAA for a zone-specific analysis of endothelial function in response to geometry and flow.

We first assessed the feasibility of using bioprinted constructs to model complex PAA geometry and the potential procedures of vessel anastomosis to nearby atretic vessels. Our in vitro model focuses on vessel sizes that would be prime candidates for such interventions, including recanalization or anastomosis.<sup>[29]</sup> To model the lack of flow in the affected vasculature and the complexity of blood flow restoration, we designed our tissue mimic to include both a patent and an atretic vessel (Figure 1A–C). To generate a reproducible analog of the patient pathology, the area of interest was isolated (white box in Figure 1C, top) and its vas-

culature geometry was translated into a simplified model that could be readily printed, incorporated into a perfusion system, and cellularized (Figure 1C, bottom). This allowed us to expand the model's utility to obtain and analyze flow patterns via ultrasound or laser PIV techniques (Figure 2). This also necessitated that we design a bioreactor housing and perfusion system that allowed us to reliably introduce biomimetic flow rates to cellularized constructs for long-term cellular assays (Figure S5, Supporting Information).

An expanding range of bioinks, such as gelMA, and the large array of modifications that they can support, have shown potential in mimicking the key characteristics of the soft tissue extracellular matrix, such as stiffness, cellular interactions, and functional remodeling over both short- and long-term assays.<sup>[30–32]</sup> In this study, we selected a bioink formulation that could create in vitro tissue models with elastic modulus (40–120 kPa, Figure 1E–H) that recapitulate what a surgical team might experience when proposing vasculature procedures (e.g., anastomosis) in vivo. In addition to high tunability, other advantages of gelMA bioinks include supporting EC adhesion and growth, adaptability to different printing modes, and availability and reliability of the bioink to eliminate a source of experimental variability.<sup>[33,34]</sup>

Although, the range of printed tissue stiffness in this study was relatively higher than the reported stiffness for native nondiseased PA (4–20 kPa<sup>[35,36]</sup>), it was well in line with those reported in various diseased PA models (e.g., 50–100 kPa in hypertensive calves<sup>[37,38]</sup>). The modulus variations observed across the width and height of printed PA constructs (Figure 1F–H) have not been reported in the native PA tissues and could be attributed to possible alterations in the hydrogel layer-by-layer crosslinking (inherent to the DLP printing process). It should be also noted that these stiffness alterations did not introduce any effect on the CFD or PIV measurements of flow hemodynamics (Figures 2–3).

The stress strain curves obtained from microindentation testes, conducted at different depth of bioprinted hydrogel constructs, demonstrated a height-dependent elastic modulus (Figure 1G). This could be attributed to the inherent nonuniformity associated with the DLP (stereolithography) bioprinting technique<sup>[39–41]</sup> that was employed to create these constructs. In such DLP/SLA methods, different layers of the solidified material are crosslinked for different durations, which could in turn result in varying stiffness/modulus along the printing axis. This was further confirmed by a heatmap, illustrating the nonuniform distribution of elastic modulus on the luminal surface of bioprinted channels (Figure 1H).

PIV flow visualization techniques, in conjunction with CFD modeling tools, provide a robust way to analyze and quantify blood (or culture media) perfusion within the established pulmonary connection in the bioprinted PA geometries. The advancement of ultrasound and laser sheet velocimetry techniques

**Figure 4.** Endothelial cell (EC) viability and proliferation within bioprinted gelMA constructs. Human ECs were manually seeded onto the luminal space in PA structures (1 mL<sup>-1</sup>) and analyzed for cell viability and growth. A) AlamarBlue assay was conducted in cast versus 3D bioprinted gelMA constructs for 35 days. AlamarBlue reduction was measured and normalized by day 1 data as baseline. B) AlamarBlue results for 3D bioprinted gelMA constructs, cultured under static versus flow, for 14 days. Measured reduction was normalized by day 1 data. A  $n = 4$ /experimental group was used for cell proliferation assays. C,D) Differences in metabolism between static ( $n = 6$ ) and perfused ( $n = 3$ ) cultures can be seen in the consumption C) and production D) of specific media components. Samples were taken on days 1, 4, 7, and 14 and subsequently analyzed using a BioProfile system. Mean concentrations of glucose C, left), glutamine C, right), lactate D, left) and glutamate D, right) are shown over time, with brackets indicating significant differences within and between groups. \* $p < 0.05$ , \*\* $p < 0.01$ , \*\*\* $p < 0.001$  and \*\*\*\* $p < 0.0001$ .

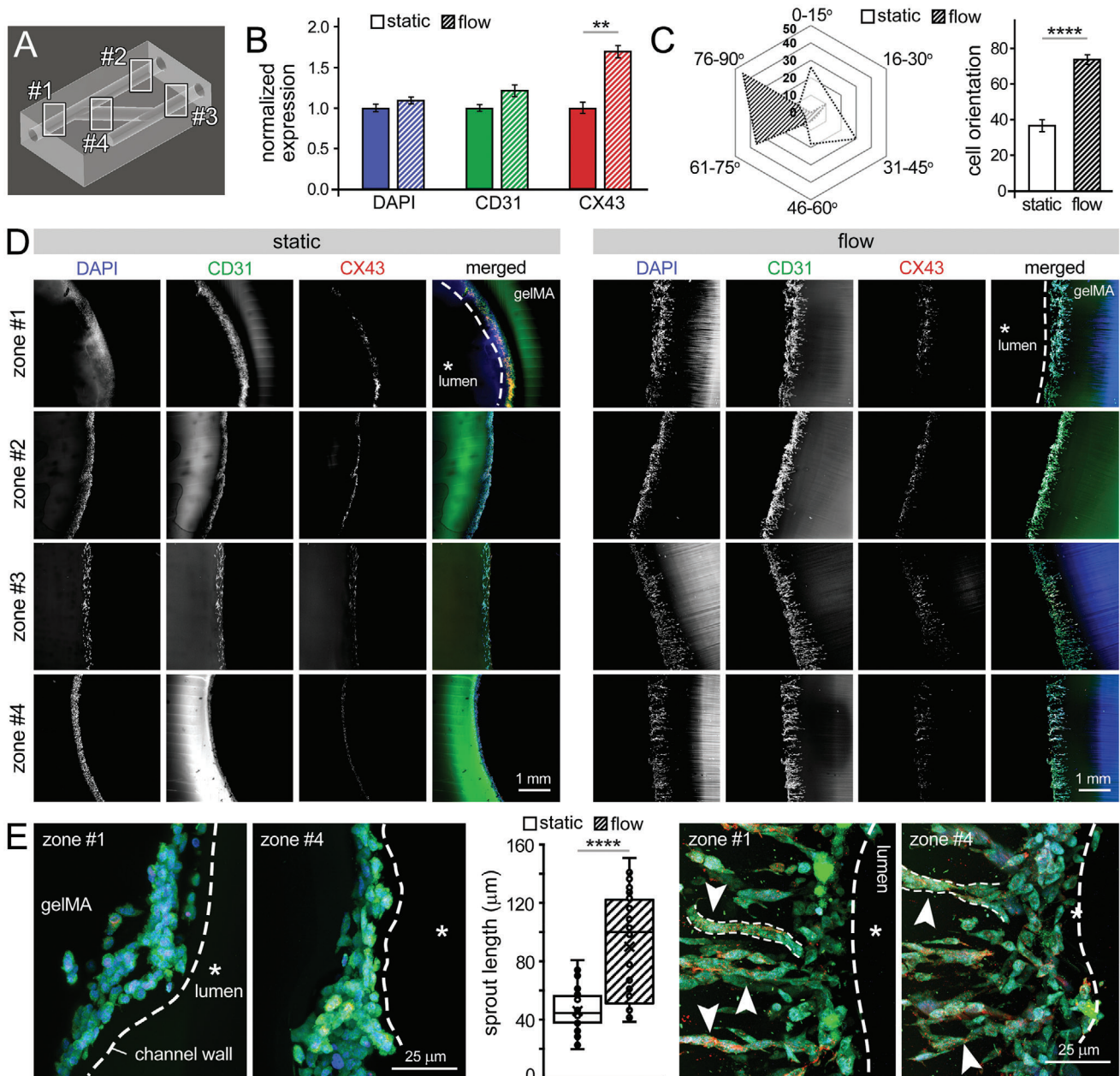


**Figure 5.** Endothelialization of bioprinted PAA constructs and the zone-specific cellular response to flow. Endothelial cells (ECs) were cultured in 3D PAA constructs for 2 weeks and then analyzed via IHC. A) Four representative zones of the construct (zones #1–4), corresponding to the 4 zones defined for wall shear stress alterations in Figure 2, were used for immunohistochemical (IHC) analysis. B) Quantification of DAPI (blue), CD31 (green) and connexin43 (red) staining in the static versus flow cultures. C) Quantification of EC alignment with respect to the printed channel axis, demonstrating a significantly different cell orientation between the two groups. D) Confocal images of the selected zones (#1–4) in static (left) versus flow (right) culture conditions, stained for DAPI nuclear marker (blue), CD31 EC-specific marker (green), and connexin43 tight junction (red). Scale bar: 1000 μm. E) Magnified representative images of zones #1 and 4 of static (left) and flow (right) culture groups, showing merged DAPI (blue), CD31 (green), and connexin 43 (red) staining. The middle graph shows quantification of sprout length obtained from the confocal images for each group. Scale bar: 100 μm. Arrows point to the ECs orienting perpendicular to the channels, forming microcapillary-like structures, and migrating inward into the gelMA tissue. A  $n = 4$ /experimental group was used for quantitative assays. \* $p < 0.05$ , \*\* $p < 0.01$ , \*\*\* $p < 0.001$  and \*\*\*\* $p < 0.0001$ .

has enabled 2D and 3D measurement of the flow hemodynamics in variety of in vitro and in vivo geometries. It is feasible to map flow dynamics at sub-millimeter scales and record the dynamic change of the flow within a tenth of a second using high frame rate 2D ultrasound imaging techniques. Full 3D flow veloc-

ity mapping, although still not available using commercial ultrasound scanners, was made possible by using recently developed 3D ultrasound velocimetry technique (Figure 2A–D)<sup>[42]</sup> and has recently been demonstrated in vivo in real-time 3D in a catheter device.<sup>[43]</sup> In previous studies with the nonreal time approach

that was also used here, our team reported accuracy of the velocity measurements as high as 95.6% even when 5% noise was added.<sup>[42]</sup> In this study, the 3D velocity was measured with a spatial sampling of 2.12 mm. To further improve the spatial resolution in future studies, a higher frequency transducer could be employed with the PAA model size reduced along the Z direction. In this study, only steady-state flow was measured using ultrasound due to the limitation of the 3D ultrasound velocimetry setup. To make a full 3D velocity map, 2D ultrasound images need to be acquired at multiple (i.e., 42 in this study) orthogonal planes under repeatable flow conditions. In the future, to measure the 3D velocity map under pulsatile flow conditions, a flow rate-gated imaging strategy could be employed by using the external trigger of the programmable ultrasound scanner.

We further expanded flow analysis of PA models using a laser PIV approach, which allowed us to recreate the full flow volume within the constructs (Figure 2E–I). The shape of the flow curves for both outlets resembled that for the inflow (Figure 2G). There was a small phase lag ( $dt = -0.02$  s or  $-6.1\%$   $T$ ) between the outlets and the inlet, while no noticeable phase difference was found between the two outlets. The momentary reversed flow velocity observed around  $t = 0.37$  s (Figure 2F,G) happened when one roller shoe detached from the tube, and it is inherent in this type of pump operating at low flow rate conditions. We did note, however, that this reversal in flow could also be seen in this particular patient population of TOF/PA/MAPCAs as the right ventricle to PA conduit becomes regurgitant.<sup>[44]</sup> In the patients that have resultant free pulmonary insufficiency, the pulse pressure becomes quite wide and results in periodic reversal of flow in the PA. Interestingly, this pulsatile pump phenomena allows us to study the effects of near free/free pulmonary insufficiency on the distal vasculature which is known to be already markedly abnormal.<sup>[44,45]</sup>

Defining eight zones within the 3D PA geometries, based on the laser PIV data, that showed greatest levels of WSS alterations (Figure 2H, Figure S3, Supporting Information) allowed us to examine the effect of flow hemodynamics on cell behavior more precisely. These zones can represent regions in the patient arteries that are clinically prone to dysregulated endothelial function and stenosis. In zone 1, at the lower wall of the inlet, the variation of the WSS synchronized with the inlet flow curve and the maximum shear appeared at the time when flowrate peaked (Figure 2H). In zones 2 and 3 near the outlets, the WSS was noticeably lower than that observed near the inlet, possibly due to lower flow rates at that region. There was a  $180^\circ$  phase difference between WSS in zones 2 and 3. In zone 4, in the conduit region, the peak WSS was the highest during the brief reversed flow phase. However, the mean WSS in zone 4 was comparable to that at the inlet.

The two PIV techniques used in this study were able to characterize in detail the changing flow patterns within the models, strongly implicating the disturbed flow as a possible trigger for restenosis within the anastomosed areas and potentially as a *de novo* cause of stenosis that is a characteristic pathology associated with anastomosed complex atretic vasculature. There was a significant overlap in the range of flow velocity measured via ultrasound PIV ( $0\text{--}4$  mm  $s^{-1}$ , Figure 2D) versus laser PIV ( $-4$  to  $8$  mm  $s^{-1}$ , Figure 2F), suggesting the accuracy and consistency of these experimental methods to measure flow hemodynamics.

In parallel to experimental flow analyses, computational platforms can greatly expand on effective validation and optimization of geometrical, structural, and flow parameters in the vascular tissue mimics.<sup>[3,46]</sup> These power complementary tools can help to address the optimal considerations of vascular anastomosis, such as diameter, location, and angle of canalization. While establishing a connection for flow may temporarily provide successful blood supply to the impacted vascular segments, stenosis-inducing flow patterns must be avoided. Otherwise, the recanalized connection may lose its patency over time or worse, can promote stenosis in the once healthy vascular segment.<sup>[47–51]</sup> For instance, low velocity, oscillatory flow patterns have been shown to correlate with arterial stenosis and thus should be avoided via proper anastomotic geometry and angle of placement, all of which are better modelled prior to the procedure. Evaluating a variety of connection designs and angles *in silico* and via techniques, such as ultrasound or laser PIV, would allow us to avoid pathologic turbulent flows that will eventually result in restenosis of the reestablish vascular tree.

The CFD analyses provided the predictions of the flow patterns in the bioprinted anastomosis at  $1\times$  and  $4\times$  scales allowing an efficient examination of the flow development in tissue constructs. Overall, CFD results were in acceptable consistency with PIV measurements and calculations for velocity and WSS, highlighting the importance of CFD simulations to efficiently predict and evaluate the effects of design parameters on flow performance (Figures 2 and 3). Interestingly, CFD results predicted the transition of parabolic velocity profiles to plug profiles as a result of the forward-reverse flow condition with velocity ranges comparable to those obtained via PIV. In general, flow was found to be laminar throughout the geometry except at the entrance of the bifurcation, where a moderate shedding of recirculation regions was observed close to peak flow acceleration and deceleration timepoints for both scales (Figure 2; Figure S4, Supporting Information). The CFD results identified zones 1 and 4 as the two important regions of consideration to avoid simultaneous high OSI and WSS. The flow recirculation regions in zone 4 led to an increase in OSI (Figure 3E) while the region prior to the bifurcation (zone 1) maintained a larger WSS with no sign of significant recirculation. Potential design parameters, such as the angulation and diameter of anastomosis between the patent and atretic arteries, can be used to modulate the amounts of WSS and OSI at the regions of consideration and reduce potential flow perturbations (Figure 4, Supporting Information). Such computational strategies could help the clinical teams in the future for more effective preplanning of interventional procedures to achieve optimal outcomes. The flow patterns in the PAA models at  $1\times$  were similar to those at  $4\times$  following (as a result of enforcing Reynolds' similarity between two scales), further corroborating CFD's potential to predict the flow hemodynamics after anastomosis (Figure S4, Supporting Information). Overall, the selective CFD studies in this work demonstrated how a personalized surgical planning platform, guided by *in vitro* modeling, and empowered by a computational optimization approach, can be developed to efficiently explore various anastomotic scenarios, and determine the best postoperative flow characteristics.

Incorporation of human ECs into the bioprinted gelMA constructs, allowed us to perform *in situ* biological analyses, such as cell viability, proliferation, and function assays (Figures 4, 5), and

link these outcomes to the mechanical and flow hemodynamics results obtained from the biomimetic 3D platforms. In comparison to the cast PA models, ECs grown in bioprinted models exhibited significantly greater levels of viability and growth (Figure 4A; Figure S6C, Supporting Information). This could be attributed to enhanced mass transport within printed constructs, due to the formation of micro porosities that are inherent to the layer-by-layer deposition of materials.<sup>[41,52]</sup> Further, the 3D printed perfused group showed a higher cell growth compared to the static prints (Figure 4B), which could mainly be due to enhanced mass transport (diffusion and convection<sup>[53,54]</sup>) and the removal of metabolic stresses on the cells as a result of flow, as confirmed by the bioprofiling analysis (Figure 4C,D).

We next evaluated the potential impact of conducting vascular stenting procedure via catheter on endothelial cells within the bioprinted PA constructs. Stented models showed significant cell activity over a two-month time span (Figure S6B,C, Supporting Information), which is within the timescale of patient pathology manifestation. Importantly, the incorporated ECs survived the mock stenting procedure (conducted day 9 in culture), were able to infiltrate the conduit, and recovered per measured metabolic activity for over 30 days poststenting (Figure S6D, Supporting Information). While we were able to demonstrate considerable cellular activity poststenting with single cellularization at the beginning of the assay, we also verified the effect of a secondary cell seeding, immediately after the stenting procedure, to simulate a potential infusion of patient-specific cells for a regenerative therapy. While there was a positive trend in cell viability and growth, there was no significant difference between the reseeded and control (single seed) groups (Figure S6D, Supporting Information). Together, these results offer a promising avenue to generating a cellular bioprinted in vitro model of PAA that can be used as a robust platform to trial novel surgical procedures, focused on stent-based therapies.<sup>[3,55,56]</sup> Future works can focus on incorporating a smooth muscle layer into the bioprinting process to mimic the bilayer vascular tissue structure.

IHC examination showed a relative (not complete) success in endothelialization of printed channels, with most areas consisting of multiple layers of cells (Figure 5). Expectedly, HUVECs showed significantly greater levels of AlamarBlue reduction in bioprinted PAA constructs cultured under flow versus static (Figure 4B), again mainly to the enhanced mass transport properties in the dynamic flow culture. In addition, altered (increased) WSS, induced by flow through the printed channels, could contribute to increased endothelial cell growth.<sup>[57,58]</sup> The latter mechanism was further confirmed by IHC analysis of the cellular PA constructs (Figure 5), where we obtained significantly greater levels of gap junction expression in the flow group. The higher CX43 expression under flow conditions could be related to cellular changes in response to increased WSS.<sup>[59,60]</sup> Remarkably, and consistent with previous findings,<sup>[61–63]</sup> ECs in perfused PA constructs oriented themselves perpendicular to flow, particularly in the zones #1 and 4 where maximum WSS were developed (Figure 5C,E). The orthogonal EC alignment in perfused samples suggested the formation of self-assembled microvasculature or neovasculature, sprouting out of the bioprinted channel toward the 3D gelMA.<sup>[64]</sup> This was further confirmed by the angiogenesis and cellular activity assay conducted on

the supernatant culture media collected from different groups (Figure S9, Supporting Information).

More in-depth quantitative analysis revealed significant differences in EC orientation along the channel walls, where zones #1 and #4 with the highest levels of WSS alterations showed the most perpendicular cell orientation to the flow (Figure S8A,B, Supporting Information). This is consistent with previous reports on perpendicular alignment of ECs in response to spatial gradients in WSS.<sup>[61]</sup> Zone-specific quantification of IHC signals also highlighted the significantly lower CD31 expression in ECs in zone #2 (the outlet 1), and lower CX43 expression in ECs in the zone #4 (within the conduit) (Figure S8C, Supporting Information). The reduced CD31 expression in the zone #2 (i.e., potential EC loss) could be attributed to the increased average WSS within that region, as predicted by the CFD results (Figure 3C), which could result in removing some of the ECs from channel surface.

The bioprofiling results indicated that HUVECs in PAA constructs cultured under flow exhibited a more efficient metabolism than those under static conditions (Figure 4C,D). These results suggest that the inclusion of a continuous flow provided a more physiologically relevant microenvironment that encouraged the cells to maintain a stable metabolism while experiencing cellular growth. It also demonstrates that the properly designed engineered tissues can recapitulate the physiological complexity of in vivo tissues/organs. Such analyses could be highly effective in the design and development of feeding strategies in future works that sustain the desirable metabolic environment.

In summary, reproducible processes to generate bioprinted patient-specific 3D models that can be used in a clinical or translational setting would be an exciting development that bridges the fields of surgical intervention and tissue engineering.<sup>[65–69]</sup> There are, however, several aspects of developed PA models that could be further improved in the future works. These include creating a complete EC coverage and an integrated endothelium with controlled permeability, precise control of endothelial layer thickness to avoid overgrowth and resulting complications, and incorporation of other vascular cells (e.g., smooth muscle cells) to improve biomimicry and function of printed arteries.

## 4. Conclusions

A multipurpose perfusable vascularized tissue platform based on the state-of-the-art 3D bioprinting and bioreactor technologies can be utilized for modeling and treatment planning of complex vascular atresia. In this model, we incorporated human endothelial cells into bioprinted designs to allow for a simplified cell-based vessel mimic. These models can be also reliably bioprinted in large numbers to allow for statistically significant multidimensional analyses. Further, the vascular mimics could be readily perfused at biomimetic flow rates. We expect our findings here to facilitate positive translational impact for the treatment of vascular stenosis in surgical and transcatheter intervention development, in pharmacological therapies, and in mapping cellular interactions. In particular, this platform can provide significant insight into the postsurgical effects on vascular function and flow modifications in bifurcation and trifurcation areas of impacted vasculature.

## 5. Experimental Section

**3D CAD Model Preparation—Validation of Patient-Inspired PA Atresia Constructs:** Starting with a patient vasculature's XA scan presenting severe case of TOF with MAPCAs, a digital 3D model (STL file) of the affected vascular system was generated using established process flow as previously described.<sup>[3]</sup> The area of interest was isolated to the clinically relevant geometry and simplified the bioprinted model to facilitate reliable and reproducible generation of a vascular bifurcation. Following STL creation, the extrapolated mimics were 3D printed in resin on a Form 3 SLA printer (Formlabs, MA, US), using the manufacturer's recommended washing and postcuring steps. Briefly, the finished models were washed for 60 min in pure isopropanol to remove residual non-crosslinked resin, followed by support removal and UV cure for 20 min to stabilize the channels' shape and harden the resin to its stable condition.

**GelMA Bioink Preparation for DLP Bioprinting:** GelMA based bioink was prepared as previously described,<sup>[70,71]</sup> but with necessary changes to reflect the use of DLP bioprinter. Briefly, porcine gelatin (Sigma) was modified with methacrylic anhydride (MAA, Sigma) at 50°C for 3 h. Functionalized gelatin was cleared of unreacted MAA via reverse osmosis, lyophilized and stored away from light at -20 °C until use.<sup>[70,71]</sup> The gelMA bioink formulation that was used to print the models constituted of 2 g of gelMA resuspended in 10 mL of sterile 1× phosphate buffered saline (PBS) for a final concentration of 20% (w/v) solution. Lithium phenyl-2,4,6-trimethylbenzoylphosphine (LAP; Sigma-Aldrich) photoinitiator was added to the solution to a final concentration of 0.5% (w/v) and the mixture was heated at 37 °C for 60 min to fully dissolve the gelMA and LAP into the PBS. Once fully dissolved, the bioink pH was adjusted to ≈7.5 and 50 μL of 300 × 10<sup>-3</sup> M Tartrazine photoabsorber (1.5 × 10<sup>-3</sup> M final concentration, Sigma) was added to allow for high-resolution DLP bioprinting with the Lumen X (CELLINK). The prepared bioink was vortexed to mix all ingredients again and further incubated at 37 °C for 5 min. This gelMA-DLP bioink was stored away from ambient light at 4 °C until ready to use, but no later than a week postpreparation. For the extrusion-based bioprinting, via a BioAssemblyBot printer (Advanced Solutions, Louisville, KY), a 20% (w/v) gelMA solution, mixed with 0.5% Irgacure photoinitiator (Sigma) was used.<sup>[3,30]</sup> To ensure adequate mechanical properties, extrusion printed constructs were crosslinked using UV light at 20 mW cm<sup>-2</sup> for 2 min.

**3D Bioprinting of PA Atresia Constructs:** Using the Lumen X bioprinter (CELLINK), 3D models of vascular bifurcation in 20% gelMA were used. The gelMA mimics were crosslinked using blue light in situ during Lumen X printing (15 s per layer; 1× burn-in; 30 ± 2 mW cm<sup>-2</sup> projector intensity), which took ≈45 min per model. These constructs comprised of a block of gelMA (25 mm × 16 mm × 8 mm) with embedded patent and stenotic vessels based on pathology presentation from patient data.<sup>[72,73]</sup> The model consisted of 2 mm channels, which is the average bifurcation vascular size for coronary arteries as well as infantile branching patterns.

**Mechanical Testing of gelMA Constructs:** Mechanical properties of bioprinted PA constructs were measured via both unconfined compression and microindentation tests (Mach-1 V500C, Biomomentum Inc., Montreal). For compression test, cubic gelMA samples were bioprinted at 5 × 5 × 5 mm<sup>3</sup> and incubated on a rocker in 1× PBS for one hour to wash out the excess non-crosslinked bioink. Subsequently, the samples underwent an unconfined compression at a displacement of 70% at 10 μm s<sup>-1</sup>. The stress-strain curve was obtained using the following equations

$$\sigma = \frac{F}{A} \quad (1)$$

$$\tau = \frac{\Delta L}{L} \quad (2)$$

where,  $\sigma$  is stress,  $F$  is the compressive force,  $A$  is the sample's cross-sectional area (Equation (1)),  $\tau$  is the compressive strain, and  $L$  is the sample height (Equation (2)). The compressive modulus was derived from the slope of the linear trend line (initial 0%–20%) of the stress-strain curve. Four replicates were tested ( $n = 4$ ) and the average value with standard deviation was recorded.

The microscale mechanical behavior of printed gelMA constructs were further assessed using microindentation (Mach-1 V500C, Biomomentum Inc.). A 500 μm probe was first used to indent on the surface of the PA constructs. Next, a vibratome (VT 1200S, Leica BioSystems) was used to slice the constructs at 4 mm depth and then another round of indentation was conducted on the channel luminal surface. All indentations were performed at a depth of 300 μm at 7.5 μm s<sup>-1</sup>, with three indentation points for each sample and a total  $n = 6$  samples. The force-displacement unloading curves were recorded and used to measure the stiffness ( $S$ ) according to the slope of the linear trend line at initial 10%–20% displacement. Reduced elastic modulus ( $E_r$ ) and plane strain modulus ( $E$ ) were derived using Equations (3)–(6)<sup>[74]</sup>

$$E_r = \frac{\sqrt{\pi}}{2\beta} \frac{S}{\sqrt{A(h_c)}} \quad (3)$$

where,  $\beta$  is a geometrical constant on the order of 1,  $S$  is the sample stiffness, and  $A(h_c)$  is projected contact area at the contact depth of  $h_c$ , which can be obtained from the equation below

$$A(h_c) = 2\pi R h_c - \pi h_c^2 \quad (4)$$

where

$$h_c = h_{\max} - \epsilon \frac{P_{\max}}{S} \quad (5)$$

where,  $h_{\max}$  and  $P_{\max}$  are the peak unloading displacement and peak unloading force, respectively, and  $\epsilon$  is a constant with a value of 0.75 for the spherical probe.<sup>[75]</sup>

The elastic modulus,  $E$ , can be then calculated using the following equation<sup>[74]</sup>

$$\frac{1}{E_r} = \frac{(1 - \nu^2)}{E} + \frac{1 - \nu_i^2}{E_i} \quad (6)$$

where,  $\nu$  and  $\nu_i$  are the Poisson's ratio of tested material and the indenter tip material, respectively (both equal 0.5).  $E_i$  represents the elastic modulus of the probe with a value of 2 GPa. All mechanical tests were performed at room temperature (≈23 °C) while hydrating the gelMA samples in 1× PBS at 37°C between measurements.

Further, the heat map of the elastic modulus ( $E$ ) of PA constructs was developed at 5 mm depth (channels luminal surface) through indentations with a 500 μm probe at a depth of 300 μm at 7.5 μm s<sup>-1</sup>. Indentation points were spaced at 2 mm intervals along each channel. The PA constructs were incubated for 15 min in 1× PBS after each of the three channels were indented to keep the samples hydrated.

**Fidelity Assessment of Bioprinted Constructs:** Bright field microscopy images were acquired at 1× and 3.2× magnifications to assess the printing fidelity in ImageJ (National Institutes of Health, USA). Design factors such as the strand diameter ratio ( $D_s$ ), strand uniformity ratio ( $U_s$ ), strand angle ratio ( $\alpha_s$ ), and interstrand area ratio ( $A_s$ ), were quantified as previously described.<sup>[30]</sup> The experimental (printed) measurement for each parameter was CAD measurement as the reference.

The bulk (macroscopic) printing fidelity was further demonstrated by assessing the printed PAA model in terms of its outer geometry and inner structural features. Geometrical factors including the length ( $l$ ), width ( $w$ ), and height ( $h$ ) of the cubic structure were measured and compared against the designed CAD model. For the inner structural details, a vibratome was used to slice the printed gelMA construct either horizontally or perpendicularly, and the structural fidelity was evaluated in terms of channel circularity ( $C = 4\pi \frac{A}{P^2}$ ), where  $A$  is the channel diameter and  $P$  is the channel periphery, and channel uniformity ( $U = \text{printed channel length}/\text{CAD channel length}$ ).<sup>[30]</sup> Three printed PAA samples ( $n = 3$ ) were used for the assessment, and tissue slices from different locations were collected for measurements.

**Cell Culture—Cellularization of Bioprinted Constructs:** HUVECs, expressing endogenous green fluorescent protein (GFP), were plated on 0.5% gelatin coated T75 flasks and maintained in complete EC Media (VascuLife VEGF Endothelial Medium Complete Kit), supplemented with pen/strep (Gibco) until they were at 90% confluency. Cell cultures were split at 1:20 and expanded fresh with full media changes every 3 days until target confluency of 90% was reached again. When passaging cells, 1 mL of 0.05% Trypsin (Invitrogen) was added to detach the cells from the flask and washed with 5 mL of HUVEC media. In a microcentrifuge tube, 100  $\mu$ L of cell solution was added to 100  $\mu$ L of Trypan Blue solution (Invitrogen), while the rest of the cell solution was transferred to a centrifuge tube. The cell-Trypan Blue solution was placed on a cell counter slide to determine the number of cells present. Once completed, the flask was washed with sterile 1 $\times$  phosphate buffered saline (PBS; Sigma-Aldrich), added 10 mL of HUVEC media and cell solution, and then stored away from light at 4 °C. Remaining cells after the split were either discarded or pelleted down for downstream experiments. In preparation for cell seeding, the cell passaging was repeated to quantify the cell number. The cell suspension was centrifuged at 1500 rpm for 5 min and resuspended in HUVEC media to reach a concentration of 1 M cells mL<sup>-1</sup>. PA atresia constructs were then seeded with HUVECs by adding 250  $\mu$ L of cell suspension into the printed patent channels and 150  $\mu$ L to the atretic channel. The cellularized models were incubated at 37 °C in complete HUVEC media for two hours to allow for cell attachment before proceeding to downstream applications. Importantly, before adding the cells, the PAA constructs were incubated overnight with 0.5% (w/v) gelatin in PBS at 37°C, to improve cell retention within the model.

**Catheter-Based Stenting of Printed PA Models:** All stenting procedures were performed in the cardiac catheterization laboratory. Two methods were used to create constructs, layer-by-layer bioprinting and casting. The bioprinted models were generated consistent with the LumenX procedure described in Methods. The cast models were made using a custom-printed mold that mimicked the vascular geometry. Following casting with gelMA and crosslinking (same as above), the cast models were removed from the molds.

It begun with unseeded constructs on day 0 of print (or casting) and created a channel between the atretic channel and the patent using a 0.14" Runthrough (Terumo) wire, followed by a Turnpike microcatheter (Teleflex). An Onyx coronary stent of 3 mm  $\times$  15 mm (Medtronic) was inflated to bridge the connection. Connections were confirmed angiographically with Omnipaque contrast. Subsequently, HUVECs were seeded ( $1 \times 10^6$  cells mL<sup>-1</sup>) into the PAA constructs to simulate the innermost vessel lining. The constructs were cultured for 56 days. In another study, HUVECs ( $1 \times 10^6$  cells mL<sup>-1</sup>) were first seeded into the PA luminal space and allowed them to recover and fully adhere to the bioprinted walls for 9 days prior to stenting. The stenting procedure was performed like above to simulate a mock interventional procedure to treat distal PAA.<sup>[3]</sup> To further help with cellularization of the stented vessels, in one study group, a secondary cell seeding was performed immediately after stenting, where another 200  $\mu$ L of  $1 \times 10^6$  cells mL<sup>-1</sup> suspension was added to the PAA constructs. The stented constructs were then tracked for at least 30 days, performing AlamarBlue assays to assess metabolic activity every 7 days.

**Bioreactor Design and Fabrication:** 3D printed polymeric housing was designed and fabricated that could incorporate the vascular gelMA models (a close fit). The perfusion chambers included one inlet and two outlets with standard barbed connectors to introduce peristaltic flow through the device with minimal damage to the construct and cellular layers within the bioprinted vessels. Fully assembled perfusion units were tested under flow to ensure that they remain leak-free and are able to handle homeostatic flow profiles at the inlet flow rate of 2 mL min<sup>-1</sup> while cells were seeded uniformly within the printed tissue mimic. This flow rate corresponds to the blood flow velocity observed in vivo in the human PAs of the same type and diameter.<sup>[3,76,77]</sup> 3D printed bioreactor holders and a media cartridge to accommodate the hybrid assembly for long-term perfusion and in situ high-throughput metabolite analysis were custom designed.

**3D PIV Analysis of Flow Hemodynamics in Bioprinted PA Models:** To conduct ultrasound (echo) PIV analysis of flow hemodynamics, an ultrasound compatible tissue-mimicking gelatin construct was fabricated

based on the 3D printed PA bifurcation model. Constructs were created using a 3D printer (Ultimaker 2+) with sacrificial polyvinyl alcohol (PVA) ink. The vascular analog was scaled up by 4 $\times$ . The model was fabricated using degassed water (91% V/V), gelatin powder (6% w/v, 300 bloom), 1-propanol (5% v/v), and 25% glutaraldehyde aqueous solution (4% v/v). The 3D printed model was placed in a plastic case with the inlets and outlets connected to tubing. The gelatin solution was poured into the case instantly after adding the glutaraldehyde. The solution solidified within 30 s with the construct embedded in it. After the gelatin analog was stored for 10 h at  $\approx$ 4 °C, water was infused through the constructs to slowly dissolve the 3D printed model, resulting in a channel with the geometry of the bifurcation inside the gelatin model. During ultrasound imaging, a constant flow rate of 8 mL min<sup>-1</sup> was introduced through the construct using a syringe pump (PHD 2000, Harvard Apparatus, Holliston, MA).

To measure the 3D flow velocity, a 3D ultrasound velocimetry method<sup>[42,46]</sup> was used in this study. A custom 3D ultrasound system was built in the lab using a custom-made rotational transducer holding device, a 3-axis motion stage (XPS-Q8, Newport, Irvine, CA, USA) and a programmable ultrasound system (Verasonics, Kirkland, WA, USA) with a linear array probe (L11-5, ATL, Bothell, WA, USA). Ultrasound contrast agents synthesized in the lab ( $\approx 10^5$  microbubbles mL<sup>-1</sup>) were used as the tracer for flow velocity measurement. 50 frames of 2D ultrasound images were acquired at 200 frames s<sup>-1</sup> at multiple orthogonal imaging planes. 2D velocity of the flow in individual planes was measured by acquiring 2D ultrasound images using a PIV algorithm.<sup>[78]</sup> A map of the full 3D flow velocity was obtained by combining 2D flow velocity vectors at the intersections of the orthogonal planes.

For laser PIV analysis, since the original (bioprinted) models were too small and nontransparent, a 4 $\times$  scaled-up design of the model was cast using transparent PDMS (Dow Corning, Sylgard-184). The 4 $\times$  scale was chosen as this was the smallest scale that the PIV methods could reliably analyze. A beaker was used as the fluid reservoir and an ultrasonic flow meter (ME 4PXL, Transonic Systems) downstream of it was used to monitor the flow rate continuously. The inlet was split into four parallel channels and ran through the four individual rollers of a peristaltic pump (VWR Variable-Speed, USA) to drive the flow circuit. The two outlets from the model returned the fluid to the beaker, closing the flow loop. To facilitate imaging of the particles in PIV experiments, a 51% by weight aqueous solution of urea<sup>[79]</sup> was used to match the refractive index (1.4134) of the PDMS. Operating at 20°C, the measured density of the solution was 1.12 g mL<sup>-1</sup> and the viscosity was 1.3cP (NDJ-5S Rotational Viscometer). The model was placed horizontally in a tank filled with the same aqueous urea solution to minimize optical distortions. During experiments, the peristaltic pump was operating at a nominal flow rate of 2 mL min<sup>-1</sup>, the same setting used in the bioprinted samples and cell culture experiments for the 1 $\times$  model. The use of four parallel channels quadrupled the nominal flow rate to 8 mL min<sup>-1</sup>, while keeping the flow waveform unchanged. With the kinematic viscosity of the working solution (1.16 cSt at 20 °C) close to that of water (1 cSt at 20 °C) and the model four times larger, the Reynolds numbers were closely matched in both experiments.

An Nd:YLF laser (DM20-527-DH, Photonics Lasers) beam was delivered by an articulated arm (LaVision 1108453) and converted to a thin sheet less than 1 mm by an adjustable sheet optics (LaVision 1108405). The laser sheet cut through the center of the flow channels in the PDMS model. The flow was seeded with 2  $\mu$ m polystyrene particles coated with Rhodamine 6G (LaVision 1001851). A CMOS high-speed camera (Phantom VEO-E 340L, 2560  $\times$  1600 px,<sup>[2]</sup> AMETEK) with a Nikon NIKKOR 105 mm Macro lens was used to record the particle fields through a 45° mounted front surface mirror. A long-pass filter (>540 nm, LaVision 1108573) mounted in front of the lens was used to block the scattered laser light by the model. The field-of-view was 76  $\times$  47 mm.<sup>[2]</sup> A total of 2000 frames of particle images were recorded at 150 frames per second and the corresponding  $\Delta t$  between images was 6.67 ms. The maximum particle displacement between frames was around 6 pixels. The particle images were processed initially by background removal and followed by a multipass cross-correlation algorithm (LaVision Davis 10). With a final interrogation window size of 16  $\times$  16 pixels and a 50% overlap, the resulting vector spacing was 0.24 mm, corresponding to 33 vectors across the

diameter of the channel. A universal outlier detection algorithm<sup>[80]</sup> was applied to remove the spurious vectors. The uncertainty of the measured velocity was around  $0.2 \text{ mm s}^{-1}$ .

To determine the WSS from the PIV data, eight different zones were defined within the 3D PA constructs. These zones were picked around the regions that showed greatest levels of shear alterations (clinically prone to dysregulated endothelial function and stenosis). First, a third-order polynomial was fitted to the velocities at four nearest points perpendicular to the wall, starting from the first nonzero velocity point. Then, the shear rate parallel to the wall was calculated by taking the first derivative of the polynomial and evaluated it at the wall. Finally, the WSS was obtained by multiplying the shear rate with the dynamic viscosity of the fluid ( $\mu = 1.3 \text{ cP}$ ). Each plotted WSS was the average of ten neighboring points parallel to the wall, minimizing the uncertainties associated with determining the exact location of the wall.

**Computational Fluid Dynamics (CFD) Modeling of Flow Hemodynamics in Bioprinted PA Constructs:** CAD geometries of vascular constructs were designed using Autodesk Fusion 360 for CFD simulations to study flow hemodynamics in bifurcated PA geometries. The bioprinted tissue models consisted of one inlet and two outlets and a conduit, resembling the placement of a connection between the patent and atretic arteries to restore the flow. Time dependent CFD simulations under a laminar flow assumption ( $\rho = 1060 \text{ kg m}^{-3}$ ) were carried out using FLUENT solver (ANSYS Inc., Lebanon, NH, USA). A volumetric flow waveform mapped to a parabolic profile and a low constant pressure were used for inlet and outlet boundaries, respectively. A rigid no-slip boundary condition was used at the entire wall sections of the model. CFD simulations were conducted at two scales: 1) the scale used for ultrasound and laser PIV analyses, referred to as 4x with inlets and outlets being 8 mm in diameter; and 2) the scale used for bioprinting (1x). The 4x simulations were used for assessing CFD predictions against PIV measurements (performed for the same dimensions) while 1x simulations, performed at a similar Reynold number, enabled them to estimate flow patterns and relevant hemodynamic results for the bioprinting scale where the PIV was measurements were not feasible. The pulsatile volumetric flow waveform was scaled to provide average inlet velocity ranging between  $\approx -7$  to  $9 \text{ mm s}^{-1}$  (for 4x), which represents a common forward-reverse flow pattern in the PA flow cycle and the blood velocity ranges normally seen in infantile PA arteries. For all simulations, fluid was considered Newtonian with a dynamic viscosity of  $1.3 \text{ mPa s}$ , consistent with the fluid properties used in PIV. In addition to the baseline conduit design used in PIV and bioprinting, CFD simulations were performed for three additional designs of the conduit, to study the effect of conduit diameter and angle on flow hemodynamics in PAA constructs.

Anisotropic discretization with tetrahedral elements was used for each model with a characteristic element length of  $0.7 \text{ mm}$  at the center and  $0.45$  at the first four layers adjacent to the wall (for 4x). Each simulation was conducted for multiple cycles (using 1000 time steps per cycle), mesh convergence was verified, and the last cycle was used for analysis. In addition to calculating velocity field, time-averaged values of the WSS magnitude and oscillatory shear index were estimated by

$$\text{TAWSS} = \frac{1}{T} \int_0^T |\text{WSS}| \, dt \quad (7)$$

$$\text{OSI} = \frac{1}{2} \left( 1 - \frac{\int_0^T \int_0^T \text{WSS} \, dt \, dt}{\int_0^T |\text{WSS}| \, dt} \right) \quad (8)$$

**Cell Viability, Bioprofiling, and Angiogenesis Assays:** HUVECs were loaded into bioprinted constructs and let adhere to the channel surfaces for 3 days before starting the metabolic and cell profiling assays. Tissue analogs were either perfused, or kept under static conditions, which allowed for noninvasive AlamarBlue assay, prepared as 10% v/v mixture with HUVEC media to measure overall metabolic activity and cell proliferation in the tissue constructs. This was performed long term for over 50 days. Cellular growth was noted to be robust over a two-week time-course and subsequent experiments under static and flow conditions were performed

over that time period. Cells were incubated in the AlamarBlue mixture for 4 h at  $37 \text{ }^\circ\text{C}$  and the 550/600 absorbance ratio was measured on a Synergy 2 plate reader (Biotek).

For bioprofiling assays, supernatants were collected from the static ( $n = 6$ ) and perfusion PAA constructs ( $n = 3$ ) throughout the culture period and analyzed ( $400 \text{ } \mu\text{L}$ ) using the BioProfile FLEX2 Automated Cell Culture Analyzer (Nova Biomedical, USA). This technique measured pH levels, metabolite concentrations (glucose, glutamine, ammonium, glutamate, lactate), and ion concentrations ( $\text{K}^+$ ,  $\text{Na}^+$ ,  $\text{Ca}^{++}$ ). Machine readouts were visualized to map out production/consumption of metabolites and changes to pH/ion concentrations during sample collection. Statistical significance was determined using single-factor ANOVA (Excel) with results considered significant at  $p < 0.05$ .

An angiogenesis cytokine assay kit (RayBiotech, Peachtree Corners, GA, USA) was used to quantify EC angiogenic activity under static versus flow conditions. Supernatants were collected from both static and flow cultures at days 1, 4, 7, and 14 ( $n = 3$ ). A  $100 \text{ } \mu\text{L}$  quantity of supernatant was used to quantify cytokine concentrations for each timepoint. The incubation protocol suggested by the supplier was used. Cytokine readouts were performed on an InnoScan 1100 Microarray Scanner (Innopsys) and their concentrations were calculated using the software provided by RayBiotech, specific to this kit.

**IHC Analysis of Cellularized PA Constructs:** Bioprinted models were perfused with HUVEC media for 14 days and then fixed in 10% formalin. Each construct was incubated in formalin overnight at  $4^\circ\text{C}$ , then washed in  $1 \times \text{PBS}$  three times for 10 min each at room temperature. Constructs were then embedded in agarose, sectioned at  $200 \text{ } \mu\text{m}$  slice thickness using a vibratome (VT 1200S, Leica BioSystems), and stored at  $4^\circ\text{C}$  until ready for IHC staining and subsequent confocal imaging. Briefly, the slices were incubated in 0.5% TritonX-100 in PBS, supplemented with 1% bovine serum albumin (BSA), for 20 min at room temperature. The slices were then washed three times with 1% BSA in PBS for 5 min at room temperature. Primary antibody against Connexin43 (mouse; Invitrogen) and CD31 (rabbit; Invitrogen) at 1:500 dilution was then incubated onto the slices overnight at  $4^\circ\text{C}$ . Anti-mouse secondary AlexaFluor647 antibody (donkey anti-mouse; Invitrogen), anti-rabbit AlexaFluor568 (donkey anti-rabbit; Invitrogen), and DAPI nuclear stain were used at 1:1000 dilution. Sectioned constructs were incubated at room temperature for 1 h, protected from light, followed by another three washes in  $1 \times \text{PBS}$  for 10 minutes each and mounted using Vectashield HardSet Antifade Mounting Medium (Vector Labs) for 15 min at room temperature. Confocal images were taken on Olympus laser scanning confocal microscope with an air 10x and 40x objectives. Epifluorescent images were also taken of GFP-positive HUVEC live cells within the PVS constructs prior to fixation using a Leica epifluorescent microscope using air 4x and 10x objectives.

**Statistical Analysis:** For AlamarBlue and bioprofiling assays, the generated data was normalized to day 1 (AlamarBlue assays only) and subsequently presented as an average  $\pm$  standard error of the mean (SEM) between replicates for each time point. One-way ANOVA or two-way ANOVA, if applicable, were used to determine if significant differences were present. A post hoc Tukey–Kramer test was performed for multiple comparisons and a  $p$ -value of  $<0.05$  was considered statistically significant ( $^*p < 0.05$ ,  $^{**}p < 0.01$ ,  $^{***}p < 0.001$ , and  $^{****}p < 0.0001$ ). At least three replicates of either static or flow PAA constructs were used for each statistical analysis in AlamarBlue metabolic assays and metabolite bioprofiling ( $n$  reported in each method section).

## Supporting Information

Supporting Information is available from the Wiley Online Library or from the author.

## Acknowledgements

The expert technical assistance and help provided by Drs. Sassan Hashemi and Timothy Slesnick in 3D reconstruction of clinical data is

acknowledged. This research was funded by the NIH grant numbers K12HD072245 and R00HL127295, Emory University School of Medicine (Pediatric Research Alliance Pilot Grant the Dean's Imagine, Innovate and Impact (I3) Research Award), and the College of Engineering at Georgia Institute of Technology, and the Marvin H. and Nita S. Floyd Research Fund Award. This research was also funded in part by R00HL138288 from the National Institutes of Health.

## Conflict of Interest

The authors declare no conflict of interest.

## Author contributions

V.S. and H.B.-H. contributed equally to this work. All authors conceived and discussed the manuscript. V.S., M.L.T., L.P., L.N., K.D., J.F., K. M., and H.D.B. designed and performed the bioprinting and cell culture experiments. M.L.T., L.P., A.T., G.K., and L.N. analyzed the data. B.J., H.C., S.I., B.D.L., D.F., and L.P.D. designed, executed, and analyzed the flow visualization assays. S.R.B., B.A.Z., and R.A. performed the computational analysis of flow. V.S., J.Z., H.D.B., and M.L.T. wrote the manuscript, and all authors edited the manuscript. V.S. and H.D.B. supervised the project.

## Data Availability Statement

Research data are not shared.

## Keywords

3D bioprinting, anastomosis, bifurcated vessels, particle image velocimetry, pulmonary artery atresia

Received: May 19, 2021

Revised: July 24, 2021

Published online:

- [1] D. I. Nikitichev, P. P., J. Avery, L. J. Robertson, T. M. Bucking, K. Y. Aris-tovich, E. Maneas, A. E. Desjardins, T. Vercauteren, *Patient-Specific 3D Printed Models for Education, Research and Surgical Simulation*, IntechOpen, London, UK **2018**.
- [2] V. Serpooshan, M. Guvendiren, *Micromachines* **2020**, *11*, 366
- [3] M. L. Tomov, A. Cetnar, K. Do, H. Bauser-Heaton, V. Serpooshan, *J. Am. Heart Assoc.* **2019**, *8*, e014490.
- [4] H. Bauser-Heaton, A. Borquez, B. Han, M. Ladd, R. Asija, L. Downey, A. Koth, C. A. Algaze, L. Wise-Faberowski, S. B. Perry, A. Shin, L. F. Peng, F. L. Hanley, D. B. McElhinney, *Circ.: Cardiovasc. Interventions* **2017**, *10*, e004952.
- [5] H. Bauser-Heaton, A. Borquez, R. Asija, L. Wise-Faberowski, Y. Zhang, L. Downey, S. B. Perry, A. Koth, L. F. Peng, C. A. Algaze, F. L. Hanley, D. B. McElhinney, *J. Thorac. Cardiovasc. Surg.* **2018**, *155*, 1696.
- [6] R. A. Ligon, D. W. Kim, R. N. Vincent, H. D. Bauser-Heaton, Y. K. Ooi, C. J. Petit, *Catheter Cardiovasc. Intervention* **2018**, *91*, 1301.
- [7] H. Bauser-Heaton, M. Ma, L. Wise-Faberowski, R. Asija, J. Shek, Y. Zhang, L. F. Peng, D. R. Sidell, F. L. Hanley, D. B. McElhinney, *Ann. Thorac. Surg.* **2019**, *107*, 1807.
- [8] X. Ma, J. Liu, W. Zhu, M. Tang, N. Lawrence, C. Yu, M. Gou, S. Chen, *Adv. Drug Delivery Rev.* **2018**, *132*, 235.
- [9] J. K. Placone, A. J. Engler, *Adv. Healthcare Mater.* **2018**, *7*, 1701161.
- [10] W. Liu, M. A. Heinrich, Y. Zhou, A. Akpek, N. Hu, X. Liu, X. Guan, Z. Zhong, X. Jin, A. Khademhosseini, Y. S. Zhang, *Adv. Healthcare Mater.* **2017**, *6*, 1601451.
- [11] W. Liu, Z. Zhong, N. Hu, Y. Zhou, L. Maggio, A. Miri, A. Fragasso, X. Jin, A. Khademhosseini, Y. S. Zhang, *Biofabrication* **2017**, *10*, 02410.
- [12] W. Liu, Z. Zhong, N. Hu, Y. Zhou, L. Maggio, A. K. Miri, A. Fragasso, X. Jin, A. Khademhosseini, Y. S. Zhang, *Biofabrication* **2018**, *10*, 024102.
- [13] P. Zhuang, W. L. Ng, J. An, C. K. Chua, L. P. Tan, *PLoS One* **2019**, *14*, e0216776.
- [14] W. Zhu, X. Qu, J. Zhu, X. Ma, S. Patel, J. Liu, P. Wang, C. S. Lai, M. Gou, Y. Xu, K. Zhang, S. Chen, *Biomaterials* **2017**, *124*, 106.
- [15] P. N. Bernal, P. Delrot, D. Loterie, Y. Li, J. Malda, C. Moser, R. Levato, *Adv. Mater.* **2019**, *31*, 1904209.
- [16] B. Grigoryan, S. J. Paulsen, D. C. Corbett, D. W. Sazer, C. L. Fortin, A. J. Zaita, P. T. Greenfield, N. J. Calafat, J. P. Gounley, A. H. Ta, F. Johansson, A. Randles, J. E. Rosenkrantz, J. D. Louis-Rosenberg, P. A. Galie, K. R. Stevens, J. S. Miller, *Science* **2019**, *364*, 458.
- [17] Z. Gu, J. Fu, H. Lin, Y. He, *Asian J Pharm. Sci.* **2020**, *15*, 529.
- [18] J. Zhang, Q. Hu, S. Wang, J. Tao, M. Gou, *Int. J. Bioprint.* **2020**, *6*, 242.
- [19] F. Pati, J. Gantelius, H. A. Svahn, *Angew. Chem., Int. Ed. Engl.* **2016**, *55*, 4650.
- [20] X. Wang, Q. Ao, X. Tian, J. Fan, Y. Wei, W. Hou, H. Tong, S. Bai, *Materials* **2016**, *9*, 23.
- [21] N. J. Mardis, *Mo. Med.* **2018**, *115*, 368.
- [22] Z. Xia, S. Jin, K. Ye, *SLAS Technol.* **2018**, *23*, 301.
- [23] K. Gold, A. K. Gaharwar, A. Jain, *Biomaterials* **2019**, *196*, 2.
- [24] S. Li, X. Tian, J. Fan, H. Tong, Q. Ao, X. Wang, *Micromachines* **2019**, *10*, 765
- [25] I. Matai, G. Kaur, A. SeyedSalehi, A. McClinton, C. T. Laurencin, *Biomaterials* **2020**, *226*, 119536.
- [26] H., Shirahama, B. H., Lee, L. P., Tan, N. J., Cho, *Sci. Rep.* **2016**, *6*, 31036.
- [27] H. Cui, S. Miao, T. Esworthy, X. Zhou, S. J. Lee, C. Liu, Z. X. Yu, J. P. Fisher, M. Mohiuddin, L. G. Zhang, *Adv. Drug Delivery Rev.* **2018**, *132*, 252.
- [28] L. Ning, R. Mehta, C. Cao, A. S. Theus, M. L. Tomov, N. Zhu, E. R. Weeks, H. Bauser-Heaton, V. Serpooshan, *ACS Appl. Mater. Interfaces* **2020**, *12*, 44563.
- [29] A. I. Elarabi, M. C. Leong, M. Alwi, *Ann. Pediatr. Cardiol.* **2017**, *10*, 203.
- [30] L. Ning, R. Mehta, C. Cao, A. Theus, M. Tomov, N. Zhu, E. R. Weeks, H. Bauser-Heaton, V. Serpooshan, *ACS Appl. Mater. Interfaces* **2020**, *12*, 44563.
- [31] J. Gopinathan, I. Noh, *Biomater. Res.* **2018**, *22*, 11.
- [32] M. L. Tomov, A. Theus, R. Sarasani, H. Chen, V. Serpooshan, in *Cardiovascular Regenerative Medicine: Tissue Engineering and Clinical Applications* (Eds: V. Serpooshan, S. M. Wu), Springer International Publishing, Cham **2019**, pp. 63–77.
- [33] K. Yue, G. Trujillo-de Santiago, M. M. Alvarez, A. Tamayol, N. Annabi, A. Khademhosseini, *Biomaterials* **2015**, *73*, 254.
- [34] M. Sun, X. Sun, Z. Wang, S. Guo, G. Yu, H. Yang, *Polymers* **2018**, *10*, 1290.
- [35] T. Bertero, W. M. Oldham, K. A. Cottrill, S. Pisano, R. R. Vanderpool, Q. Yu, J. Zhao, Y. Tai, Y. Tang, Y. Y. Zhang, S. Rehman, M. Sugahara, Z. Qi, J. Gorcsan 3rd, S. O. Vargas, R. Saggarr, R. Saggarr, W. D. Wallace, D. J. Ross, K. J. Haley, A. B. Waxman, V. N. Parikh, T. De Marco, P. Y. Hsue, A. Morris, M. A. Simon, K. A. Norris, C. Gaggioli, J. Loscalzo, J. Fessel, S. Y. Chan, *J. Clin. Invest.* **2016**, *126*, 3313.
- [36] Z. Wang, R. S. Lakes, M. Golob, J. C. Eickhoff, N. C. Chesler, *PLoS One* **2013**, *8*, e78569.
- [37] S. R. Lammers, P. H. Kao, H. J. Qi, K. Hunter, C. Lanning, J. Albietz, S. Hofmeister, R. Mecham, K. R. Stenmark, R. Shandas, *Am. J. Physiol.: Heart Circ. Physiol.* **2008**, *295*, H1451.
- [38] M. J. Golob, D. M. Tabima, G. D. Wolf, J. L. Johnston, O. Forouzan, A. M. Mulchrone, H. B. Kellihan, M. L. Bates, N. C. Chesler, *J. Biomech.* **2017**, *55*, 92.

- [39] M. Nowicki, A. Richter, B. Wolf, H. Kaczmarek, *Polymer* **2003**, *44*, 6599.
- [40] A. S. Theus, L. Ning, B. Hwang, C. Gil, S. Chen, A. Wombwell, R. Mehta, V. Serpooshan, *Polymers* **2020**, *12*, 2262.
- [41] L. Ning, C. J. Gil, B. Hwang, A. S. Theus, L. Perez, M. L. Tomov, H. Bauser-Heaton, V. Serpooshan, *Appl. Phys. Rev.* **2020**, *7*, 041319.
- [42] X. Zhou, V. Papadopoulou, C. H. Leow, P. Vincent, M.-X. Tang, *Ultrasound Med. Biol.* **2019**, *45*, 795.
- [43] B. D. Lindsey, B. Jing, S. Kim, G. C. Collins, M. Padala, *Ultrasound Med. Biol.* **2020**, *46*, 2560.
- [44] J. B. Lakier, P. Stanger, M. A. Heymann, J. I. Hoffman, A. M. Rudolph, *Circulation* **1974**, *50*, 167.
- [45] K. G. Blyth, R. Syed, J. Chalmers, J. E. Foster, T. Saba, R. Naeije, C. Melot, A. J. Peacock, *Respir. Med.* **2007**, *101*, 2495.
- [46] A. D. Cetnar, M. L. Tomov, L. Ning, B. Jing, A. S. Theus, A. Kumar, A. N. Wijntjes, S. R. Bhamidipati, K. P. Do, A. Mantalaris, J. N. Os-hinski, R. Avazmohammadi, B. D. Lindsey, H. D. Bauser-Heaton, V. Serpooshan, *Adv. Healthcare Mater.* **2020**, e2001169. <https://doi.org/10.1002/adhm.202001169>
- [47] M. Ziyrek, A. L. Sertdemir, M. Duran, *J Saudi Heart Assoc.* **2020**, *32*, 399.
- [48] N. Galanakis, N. Kontopodis, S. Charalambous, S. Palioudakis, I. Kak-isis, G. Geroulakos, D. Tsetis, C. V. Ioannou, *Ann. Vasc. Surg.* **2020**, *73*, 385.
- [49] S. Kamangar, I. Anjum Badruddin, A. E. Anqi, C. Ahamed Saleel, V. Tirth, T. M. Yunus Khan, M. Anas Khan, Z. Mallick, N. J. Salman Ahmed, *Bio-Med. Mater. Eng.* **2020**, *31*, 339.
- [50] D. G. Katritsis, I. Pantos, T. Zografos, A. Spahillari, A. de Waha, A. Kopanidis, S. Foussas, P. H. Stone, A. Kastrati, D. Cutlip, *Am. J. Car-diol.* **2021**, *141*, 7.
- [51] N. Saito, Y. Mori, T. Komatsu, *Med. Devices* **2020**, *13*, 365.
- [52] F. Watson, J. Maes, S. Geiger, E. Mackay, M. Singleton, T. McGravie, T. Anouilh, T. D. Jobe, S. Zhang, S. Agar, S. Ishutov, F. Hasiuk, *Transp. Porous Media* **2019**, *129*, 449.
- [53] N. Salehi-Nik, G. Amoabediny, B. Pouran, H. Tabesh, M. A. Shokr-gozar, N. Haghighipour, N. Khatibi, F. Anisi, K. Mottaghy, B. Zandieh-Doulabi, *Biomed Res. Int.* **2013**, *2013*, 762132.
- [54] N. K. Mekala, R. R. Baadhe, R. Potumarthi, *Asia-Pac. J. Chem. Eng.* **2014**, *9*, 318.
- [55] M. L. Tomov, B. Jing, A. Kumar, K. Do, A. Cetnar, S. R. Bhamidi-pati, L. Perez, N. Panoskaltis, T. C. Slesnick, R. Avaz, A. Mantalaris, B. Lindsey, H. Bauser-Heaton, V. Serpooshan, *Circ. Res.* **2020**, *127*, A405.
- [56] V. Serpooshan, M. L. Tomov, A. Kumar, B. Jing, S. R. Bhamidipati, N. Panoskaltis, R. Avaz, T. C. Slesnick, A. Mantalaris, B. Lindsey, H. Bauser-Heaton, *Circ. Res.* **2020**, *127*, A427.
- [57] J. M. Dolan, H. Meng, S. Singh, R. Paluch, J. Kolega, *Ann. Biomed. Eng.* **2011**, *39*, 1620.
- [58] D. A. Chistiakov, A. N. Orekhov, Y. V. Bobryshev, *Acta Physiol.* **2017**, *219*, 382.
- [59] J. E. Gabriels, D. L. Paul, *Circ. Res.* **1998**, *83*, 636.
- [60] N. DePaola, Davies, P. F., W. F. Pritchard Jr., L. Florez, N. Harbeck, D. C. Polacek, *Proc. Natl. Acad. Sci. USA* **1999**, *96*, 3154.
- [61] E. Michalaki, V. N. Surya, G. G. Fuller, A. R. Dunn, *Commun. Biol.* **2020**, *3*, 57.
- [62] R. Sinha, S. Le Gac, N. Verdonshot, A. van den Berg, B. Koopman, J. Rouwkema, *Sci. Rep.* **2016**, *6*, 29510.
- [63] C. Wang, B. M. Baker, C. S. Chen, M. A. Schwartz, *Arterioscler., Thromb., Vasc. Biol.* **2013**, *33*, 2130.
- [64] N. Mori, Y. Akagi, Y. Imai, Y. Takayama, Y. S. Kida, *Sci. Rep.* **2020**, *10*, 5646.
- [65] V. Serpooshan, M. Zhao, S. A. Metzler, K. Wei, P. B. Shah, A. Wang, M. Mahmoudi, A. V. Malkovskiy, J. Rajadas, M. J. Butte, D. Bernstein, P. Ruiz-Lozano, *Biomaterials* **2013**, *34*, 9048.
- [66] V. Serpooshan, P. Ruiz-Lozano, *Methods Mol. Biol.* **2014**, *1210*, 239.
- [67] V. Serpooshan, M. Zhao, S. A. Metzler, K. Wei, P. B. Shah, A. Wang, M. Mahmoudi, A. V. Malkovskiy, J. Rajadas, M. J. Butte, D. Bernstein, P. Ruiz-Lozano, *Bioengineered* **2014**, *5*, 193.
- [68] K. Wei, V. Serpooshan, C. Hurtado, M. Diez-Cunado, M. Zhao, S. Maruyama, W. Zhu, G. Fajardo, M. Nosedá, K. Nakamura, X. Tian, Q. Liu, A. Wang, Y. Matsuura, P. Bushway, W. Cai, A. Savchenko, M. Mahmoudi, M. D. Schneider, M. J. van den Hoff, M. J. Butte, P. C. Yang, K. Walsh, B. Zhou, D. Bernstein, M. Mercola, P. Ruiz-Lozano, *Nature* **2015**, *525*, 479.
- [69] M. Mahmoudi, M. Yu, V. Serpooshan, J. C. Wu, R. Langer, R. T. Lee, J. M. Karp, O. C. Farokhzad, *Nat. Nanotechnol.* **2017**, *12*, 845.
- [70] H. Shirahama, B. H. Lee, L. P. Tan, N. J. Cho, *Sci. Rep.* **2016**, *6*, 31036.
- [71] H. Cui, S. Miao, T. Esworthy, X. Zhou, S. J. Lee, C. Liu, Z. X. Yu, J. P. Fisher, M. Mohiuddin, L. G. Zhang, *Adv. Drug Delivery Rev.* **2018**, *132*, 252.
- [72] D. R. Holmes Jr., K. H. Monahan, D. Packer, *JACC Cardiovasc. Inter-vention* **2009**, *2*, 267.
- [73] C. Hassani, F. Saremi, *Radiographics* **2017**, *37*, 1928.
- [74] W. C. Oliver, G. M. Pharr, *J. Mater. Res.* **2004**, *19*, 3.
- [75] W. C. Oliver, G. M. Pharr, *J. Mater. Res.* **1992**, *7*, 1564.
- [76] J. M. Jouannic, D. Bonnet, A. A. Hislop, R. Roussin, A. T. Dinh-Xuan, *Pediatr. Res.* **2004**, *56*, 385.
- [77] Y. Kawahira, H. Kishimoto, H. Kawata, S. Ikawa, H. Ueda, T. Naka-jima, F. Kayatani, N. Inamura, T. Nakada, *J. Cardiovasc. Surg.* **1997**, *12*, 253.
- [78] W. Thielicke, E. Stamhuis, *J. Open Res. Software* **2014**, *2*, e30.
- [79] M. C. Brindise, M. M. Busse, P. P. Vlachos, *Exp. Fluids* **2018**, *59*, 1.
- [80] J. Westerweel, F. Scarano, *Exp. Fluids* **2005**, *39*, 1096.